

# High Power and Highly Linear Monolithically Integrated Distributed Balanced Photodetectors

M. Saif Islam, *Member, IEEE, Member, OSA*, Thomas Jung, *Student Member, IEEE*, Tatsuo Itoh, *Fellow, IEEE*, Ming C. Wu, *Senior Member, IEEE, Member, OSA*, Antonino Nespola, Deborah L. Sivco, and Alfred Y. Cho, *Fellow, IEEE*

**Abstract**—A distributed balanced photodetector with high saturation photocurrent and excellent linearity has been experimentally demonstrated. The maximum linear direct current (dc) photocurrent of 33 mA per branch is equivalent to 66 mA in single-ended photodetectors. A setup for investigating the alternating current (ac) linearity of the receiver is proposed and experimentally demonstrated. The receiver exhibits high ac linearity, even under high power operation. The bandwidth of the receiver remains unchanged when the effective dc photocurrent is varied from 1 mA to 21 mA. The distribution of photocurrents was also measured. Device length for optimum radiofrequency (RF) performance is calculated and implemented in the design. A correlation between the dark current of the photodiodes and their failure mechanism has been established. Analyzing the failure mechanism, junction diodes are found to be more suitable for high power applications.

**Index Terms**—Analog fiber optic links, balanced photodetectors, failure mechanism, high photocurrent, high power photodiodes, metal–semiconductor–metal (MSM), microwave photonics, optical receivers, p-i-n, radiofrequency (RF) photonics.

## I. INTRODUCTION

**B**ALANCED receivers are very attractive for high performance microwave photonic links. They can suppress the laser relative intensity noise (RIN) and the amplified spontaneous emission noise (ASE) from erbium-doped fiber amplifiers (EDFA) [1], [2]. This enables the link to achieve shot noise-limited performance at high optical powers. The link gain, spurious-free dynamic range (SFDR), and noise figure are greatly improved. To realize these advantages, balanced photodetectors with high saturation photocurrents and broad bandwidth are needed. Broad-band, high power balanced detectors are also gaining increasing applications in spectroscopy, ellipsometry, and biomedical image processing. Previously, we demonstrated a novel monolithic distributed

balanced photodetector [3] in the InP–InGaAs material system using velocity-matched distributed photodetectors (VMDP) [4]. It consists of several pairs of balanced photodiodes (PDs) connected by passive optical waveguides (WGs). The difference photocurrents are coherently superimposed. This approach allows enlarged absorption volume without sacrificing the bandwidth. We have also demonstrated broad-band suppression (1–12 GHz) of common-mode noises [5]. Maximum noise suppression of 36 dB was observed at the relaxation oscillation frequency of a distributed feedback (DFB) laser. Significant improvement of signal-to-noise ratio (SNR) has been observed over a wide range of frequencies and phase mismatch of input radiofrequency (RF) signals. Although velocity matching was achieved by slowing down the chirped-pulse wavelength (CPW) with proper distribution of PDs, good power distribution was not achieved because of poor waveguide characteristics. Thus, the maximum direct current (dc) photocurrent was limited to 12 mA and the alternating current (ac) linearity under high power operation has not been demonstrated.

In this paper, we report on an improved distributed balanced photodetector with continuous optical WG and strong optical confinement. It exhibits superior dc and ac linearity as well as a higher linear photocurrent of 33 mA (equivalent to 66 mA from regular, nonbalanced photodetectors). We have investigated the ac linearity of devices under high power operation. The bandwidth of the receiver is found to remain unchanged even under high optical illumination. The distribution of photocurrents was also measured for the first time. The distributed detection is shown to be very important for high saturation photocurrents. Device length for optimum RF performance is calculated and implemented in the design. We have also investigated the role of dark currents on the failure mechanism of high power PDs. We found that a junction diode such as p-i-n offers some fundamental advantages for high power photodetectors.

## II. DEVICE DESIGN, OPTIMIZATION, AND DC PERFORMANCE

Fig. 1 shows the scanning electron micrograph (SEM) of the distributed balanced photodetector. It consists of two input optical WGs, two linear arrays of metal–semiconductor–metal (MSM) PDs distributed along the passive optical WGs, and a 50- $\Omega$  CPW microwave transmission line. The detector operates in balanced mode when a bias voltage is applied between the two ground electrodes of the CPW. The common-mode photocurrent flows directly to the ground electrode while the difference photocurrent (signal) flows to the center conductor.

Manuscript received November 29, 2000; revised October 2, 2001. This project was supported in part by the Office of Naval Research (ONR) under a Multi-University Research Initiative (MURI) on radiofrequency photonics, and the University of California Microelectronics Innovation and Computer Research Opportunities (UC MICRO).

M. S. Islam was with the Electrical Engineering Department, University of California at Los Angeles (UCLA), Los Angeles, CA 90095-1594 USA. He is now with Gazillion Bits, Inc., San Jose, CA 95134 USA (e-mail: saif@ieee.org).

T. Jung, T. Itoh, and M. C. Wu are with the University of California at Los Angeles (UCLA), Electrical Engineering Department, Los Angeles, CA 90095-1594 USA (e-mail: wu@ee.ucla.edu).

A. Nespola is with Optical Technologies Italia (OTI), R&D Department, Milano 20126, Italy.

D. L. Sivco and A. Y. Cho are with Lucent Technologies, Bell Laboratories, Murray Hill, NJ 07974 USA.

Publisher Item Identifier S 0733-8724(02)00466-8.

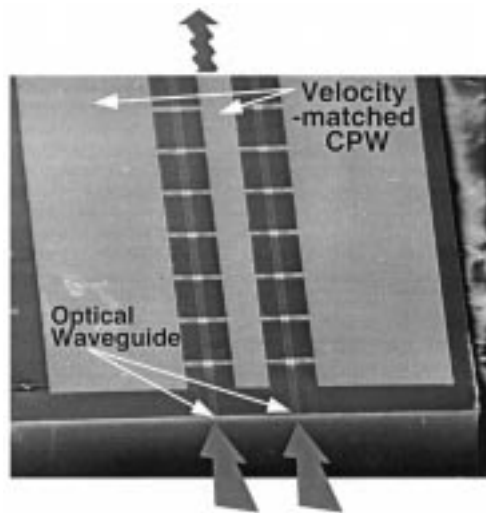


Fig. 1. SEM micrograph of the distributed balanced photodetectors. Two arrays of high-speed MSM PDs are distributed along one pair of optical waveguides and a 50- $\Omega$  CPW microwave transmission line.

The signal is then collected by the CPW. The diodes are 20- $\mu\text{m}$  long and 5- $\mu\text{m}$  wide. The separation between PDs is 100  $\mu\text{m}$ . The MSM fingers with 1- $\mu\text{m}$  width and 1- $\mu\text{m}$  spacing are patterned by optical lithography. The central conductor of the CPW has a width of 60  $\mu\text{m}$  and the separation between the central conductor and the ground conductors is 90  $\mu\text{m}$ . The optical WG are separated by 150  $\mu\text{m}$ . Without the PDs, the velocity of the CPW is more than 30% faster than the light velocity in the optical WG. The PD arrays provide periodic capacitance loading to slow down the microwave velocity. By adjusting the length and separation of the PDs, velocity matching between the CPW and the optical WGs is achieved. The PDs are designed to operate below saturation under high optical input by coupling only a small fraction of light from the passive WG to each individual PD.

The optical waveguide consists of a 200-nm-thick  $\text{In}_{0.52}\text{Al}_{0.37}\text{Ga}_{0.11}\text{As}$  lower cladding layer, a 500-nm-thick  $\text{In}_{0.52}\text{Al}_{0.178}\text{Ga}_{0.302}\text{As}$  core region, a 200-nm-thick  $\text{In}_{0.52}\text{Al}_{0.37}\text{Ga}_{0.11}\text{As}$  first upper cladding layer, and a thin  $\text{In}_{0.52}\text{Al}_{0.48}\text{As}$  second upper cladding layer. The 150-nm-thick absorption region is located on top of the waveguide for evanescent coupling. Because the Schottky barrier height of most metals on InGaAs is typically 0.2–0.3 eV, and  $\text{In}_{0.52}\text{Al}_{0.48}\text{As}$  cap layer is used to increase the Schottky barrier height and, therefore, decrease the dark current of the photodiodes. A graded layer is incorporated in the structure to reduce the minority carrier trapping at the InAlAs–InGaAs band edge discontinuity.

Two types of devices—wide mesa and continuous mesa—were fabricated; both are shown in Fig. 2. There is a tradeoff between the difficulty levels in the fabrication process and the overall performance of these two types of devices. The wide-mesa devices help eliminating the risk of MSM finger discontinuity fabricated on a nonplanar surface topology. Although MSM PDs are relatively easy to fabricate, the process of making continuous metal fingers along the lateral direction of a rib WG is a challenging task because metal fingers are expected to run down the active PD mesa in order to

eliminate low field regions. When bandwidth above 100 GHz is targeted, MSM fingers are  $\sim 100$  nm in width. In order to ensure continuity of such narrow metal fingers, planarity of the surface is an important precondition. Keeping this in mind, we fabricated our wide-mesa balanced receivers with MSM PDs that are placed on 10- $\mu\text{m}$ -wide mesas to ensure ease in the fabrication processes. A 3- $\mu\text{m}$ -wide shallow single-mode rib WG was employed to serially connect the wide mesa PDs. Shallow waveguide with a rib height of 0.2  $\mu\text{m}$  helps to ensure the continuity of the metal interconnects without surface planarization. Fig. 2(a) shows the way wide-mesa PDs are connected to the optical WG in the balanced receiver.

Although designing the active PD mesas wider than the passive WG in our wide-mesa receiver facilitated the fabrication of thin MSM fingers, it introduced excessive optical loss in WG-PD interface regions because of the discontinuity in the lateral widths. All of the input power in the wide-mesa device propagates in the fundamental mode in the passive WG and suffers a loss when it enters the multimode active PD region [6]. In addition to the loss in the wide-mesa region, the laterally single-mode shallow-ridge WG also contributes to optical loss due to coupling to slab modes. When individual PD responsivity in the receiver was measured, most of the input power was found to go to the first few pairs of PDs in the wide-mesa receiver. Fig. 3 shows the responsivity of each PD in each array. As is evident from the figure, almost all of the power is absorbed by the first few PDs and the rest are underused or not used at all. Thus, the discontinuity in the width of the active mesa and passive WG resulted in a poor guiding of the input power, which severely hampered the distributed detection scheme. The observed DC saturation power level of the wide-mesa receivers was, in fact, the power level of the first pair of PDs. We measured only 12 mA of linear photocurrent from each branch in those wide-mesa balanced receivers [5]. Our detailed simulation on the wide-mesa receivers are also consistent with the experimentally observed performance.

Unlike the wide-mesa devices, the continuous-mesa devices are more suitable for delivering the optical power to multiple PDs in each array. In the wide-mesa receiver, this could not be realized successfully. In order to realize truly distributed detection, we introduced two basic improvements to optimize the performance of this device. These are continuous WG transitions between passive waveguide and active PDs, and *laterally* multimode optical WGs. In the *continuous mesa devices*, we used the same device epistucture as in the wide-mesa device, but employed a 1.5- $\mu\text{m}$  *deep ridge* strong index-guided, and 5- $\mu\text{m}$ -wide *laterally multimode optical waveguide*. The coupling losses at waveguide transitions are greatly reduced by maintaining uniform width for both the active PD and the passive waveguide, and power is smoothly guided to many distant PDs. Once better guiding is achieved, saturation photocurrent of the whole structure improves because of the contribution of many PDs rather than only the first few PDs in each array, which was the case with our wide-mesa devices. This is how laterally multimode waveguide helps improve the saturation current in our device.

Although all of these improvements greatly enhanced the device performance, the fabrication of continuous metal fingers across the 1.5- $\mu\text{m}$ -high WG became a challenging issue. Partic-

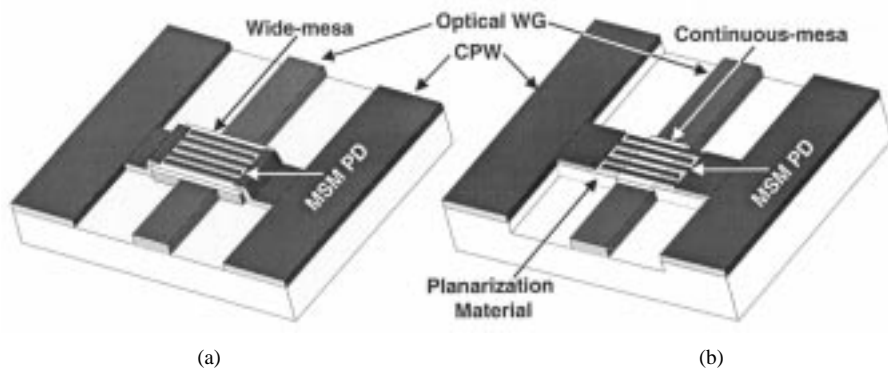


Fig. 2. (a) Active PD region of a wide-mesa device. A pair of 3- $\mu\text{m}$ -wide shallow single-mode rib waveguide serially connects the wide-mesa PDs. The discontinuity in the mesa width results in an excessive optical loss at the waveguide transitions, and only the first pair of PDs had been effectively illuminated. (b) Active PD region of a continuous-mesa device. A planarization material is required to ensure the continuity of the MSM fingers.

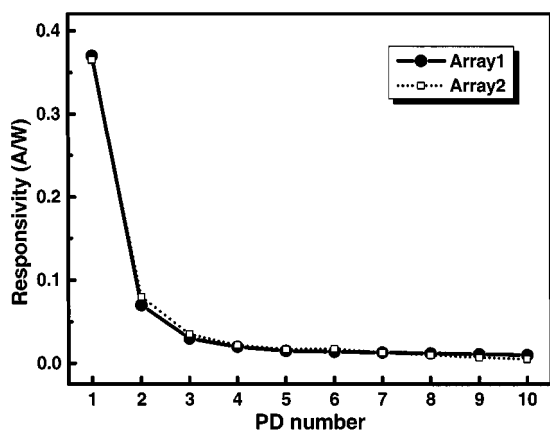
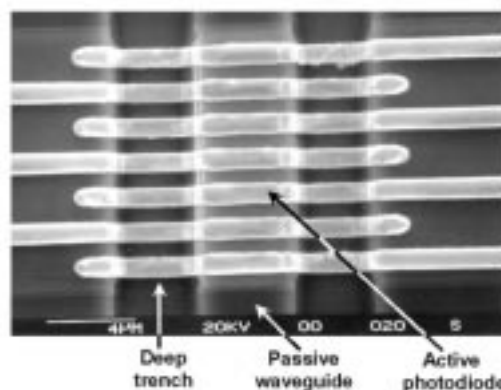
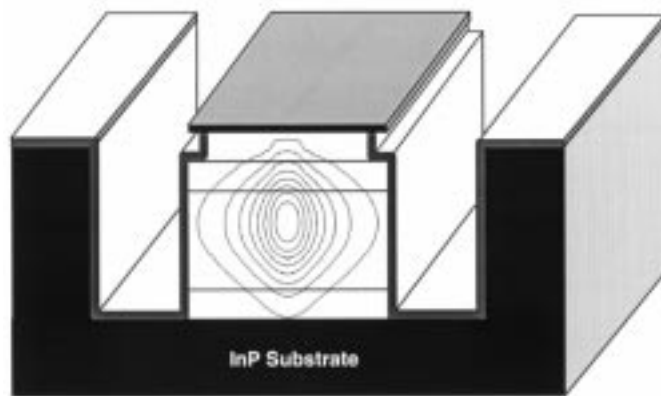


Fig. 3. Responsivity of individual PDs in two arrays of wide-mesa distributed balanced receivers. Almost all of the power is absorbed by the first PD and the rest remain underused. The first diode fails early and shows nonlinearity with little photocurrent.



(a)



(b)

Fig. 4. (a) Close-up view of an MSM PD on top of an optical waveguide. The passive WG and active PDs are continuous in width. (b) Cross section of the active PD region. Two deep trenches are fabricated to define the waveguide. These trenches need to be planarized in order to ensure the continuity of the MSM fingers. Most of the input power is confined to the WG core and only a small fraction of it is coupled to the absorption layer of the PD.

ular care has been taken to ensure the continuity of the MSM fingers across the nonplanar active PD region, as shown in Fig. 4. By applying some planarization mechanisms, the continuity of the fingers can be maintained. Polymethylglutarimide (PMGI) or benzocyclobutene (BCB) are among the planarization materials most widely used. As high power operation is likely to generate huge heat in the vicinity of PDs, PMGI might degrade in such physical conditions. BCB is the more appropriate choice for such applications. Fig. 4(b) shows the trenches around the optical WG that must be planarized in order to run thin MSM fingers across those. In the rest of the paper, we present the dc and RF performance of this continuous-mesa device.

In the fabrication process of the receiver, PD mesas were isolated by etching away the active layers from the wafer except from the places where PDs are located. A plasma-enhanced chemical-vapor deposition (PECVD) silicon nitride ( $\text{Si}_3\text{N}_4$ ) etch mask was then used for  $\sim 1.5\text{-}\mu\text{m}$  deep WG etching. After defining  $5\text{-}\mu\text{m}$ -wide multimode WGs,  $\text{Si}_3\text{N}_4$  was removed using buffered hydrogen fluoride (HF) oxide etch (BOE). A thin PECVD  $\text{Si}_3\text{N}_4$  film of  $1500\text{-}\text{\AA}$  thickness was then deposited all over the sample to achieve three purposes. First, it covers the mesa walls and, thus, prevents the metal fingers from touching the InGaAs layer, which causes a very low Schottky barrier and high dark currents. Second, it passivates the surface of the

wafer; finally, the fingertips of the MSM photodiodes and the CPW are placed on the top of the dielectric layers so that soft breakdown can be prevented and dark current contributions from the CPW can be eliminated [7]. The active regions of the PDs were defined by opening  $5 \times 20 \mu\text{m}^2$  windows on a  $150\text{-nm}$ -thick  $\text{Si}_3\text{N}_4$  film using HF BOE. The Ti–Au electrodes and contact pads were then delineated by standard liftoff process. Immediately before the metal evaporation, the sample

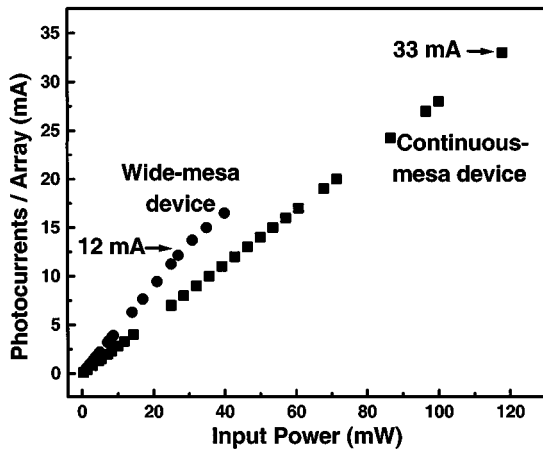


Fig. 5. dc photocurrent versus input power for both wide-mesa and continuous-mesa devices. The dc photocurrent remains linear up to 33 mA in the structure with continuous-mesa device. Wide-mesa devices exhibit much lower linear photocurrents of 12 mA. Both PDs are biased at 4 V.

is treated twice with 4% HF to make sure that no oxide layer degrades the Schottky contact. A thick coplanar waveguide was formed by standard liftoff process to connect the distributed balanced photodetectors. The fabrication of the device was especially designed to suppress the dark current of the receiver. Later, in Section IV, we will discuss the correlation between the dark current of a PD and the photocurrents at its failure.

The continuous-mesa devices resulted in very good dc and ac linearity. The receiver with a continuous multimode WG showed almost threefold improvement in the maximum photocurrent level with respect to wide-mesa single mode WG devices reported in [5]. Fig. 5 shows measured photocurrent in one branch of the PD versus the input optical power. The photocurrent remains linear up to 33 mA when biased at 4 V. It should be noted that the 33-mA photocurrent in a balanced photodetector is equivalent to 66-mA photocurrent in a single-ended photodetector because the RF signals from both branches of the PD's add-in phase. The device fails at higher photocurrent due to thermal runaway [8]. In most cases, the first two diodes in each row were affected by local increase of temperature that accelerates the diffusion of contact metal into semiconductor layers. Energy dispersive X-ray analysis (EDX) has shown evidence of such a process [8]. Measurements were made at lower voltage (i.e., 2.6 V) to investigate nonlinearities at high power. We did not observe any such nonlinearities in the measured photocurrent. For comparison, the photocurrent data from the wide-mesa devices is also plotted in the same figure. The maximum linear photocurrent (12 mA) of these devices is much lower than that of the continuous-mesa devices. Also, in contrast to the continuous-mesa devices, the photocurrent in the wide-mesa devices becomes nonlinear before it reaches catastrophic damage. This indicates that most of the photocurrent in our wide-mesa devices was contributed by the first few PDs (as is shown in Fig. 3). By employing a continuous multimode WG in our present structure, the input power is more effectively delivered to all of the PDs in each array. Please note that although the linear photocurrents improved in this optimized design, the thermal effect ultimately limits the

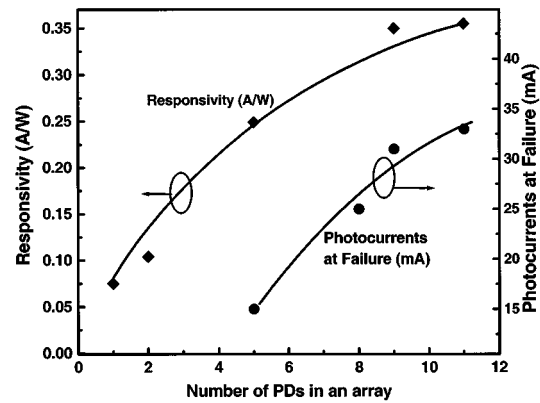


Fig. 6. Measured responsivity and dc photocurrents versus number of PDs in each array of the continuous-mesa balanced receivers. The solid lines are generated using a theoretical model that used the experimentally obtained data points.

maximum photocurrent of the receiver. In Section IV, we will investigate the thermal failure issues and show how, using p-i-n PDs, the receiver photocurrent performance can be further improved.

The distribution of photocurrent in the distributed balanced receiver is also investigated experimentally. We cleaved receivers into many different sizes consisting of different numbers of balanced PD pairs. We then measured the responsivities of each receiver. The receiver input power was increased until we reached the failure photocurrents. All of the receivers were found to fail with varying linear photocurrents. When the responsivity and photocurrents versus number of PDs in a receiver are plotted, we find that the input power is very well guided to multiple PDs in each array. Fig. 6 shows dc responsivity versus different numbers of PDs in the receiver. The characteristic of distributed detection is evident from the figure. The responsivity of the receiver increases steadily with increasing number of PDs. The figure gives an indication of better guiding of input power to multiple PDs compared to that of the wide-mesa devices shown in Fig. 3. The right axis of Fig. 6 also plots the highest photocurrent attained in these receivers with different lengths before they failed. It is important to notice that both responsivity and photocurrents reach saturation levels with 12 PDs in a receiver. Subsequent PDs in the receiver remain unused.

If the failure photocurrent of the first PD of each type of devices is compared, the wide-mesa devices are found to survive a photocurrent of around 16 mA, whereas the continuous-mesa device fails with a photocurrent of 7 to 8 mA (Fig. 6). This is mainly caused by the difference in the power dissipation per unit area in these two types of devices. In the wide-mesa device, the width of the passive waveguide is  $3\text{-}\mu\text{m}$  and the active PD region is more than  $10\text{-}\mu\text{m}$ . Several higher order modes are excited in the active photodiode region of the wide-mesa device as the single-mode input power propagates from the narrow passive waveguide into the wide mesa region and power per unit volume reduces to a lower level in the active absorption layer. When the unabsorbed power couples back to the passive waveguide, the discontinuity in the interface causes considerable loss. Thus, a large fraction of the input power in the wide-mesa device is

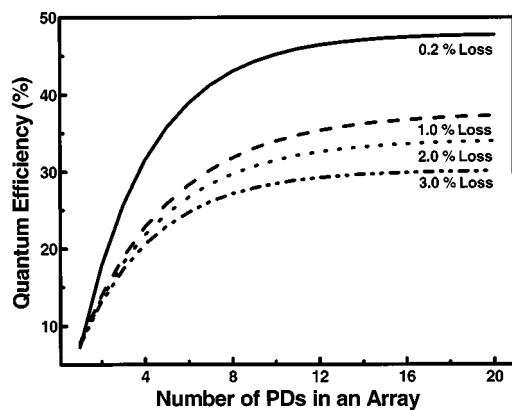


Fig. 7. Simulated quantum efficiency (QE) with different magnitude of loss coefficients per period (one period consists of a passive waveguide and two PD-waveguide interfaces). The lowest curve in the figure corresponds to 3% loss per period and a quantum efficiency of  $\sim 28\%$ , which is the experimentally observed QE of our receiver.

found to be absorbed by the first PD in the array. However, because of power dilution in a wide area, absorption of input power per unit volume remains low, resulting in low heat dissipation per unit area. On the other hand, all of the lateral modes in a continuous-mesa device are confined to narrower ( $5\text{-}\mu\text{m}$ ) width. Hence, absorption per unit volume and heat dissipation per unit area is higher, and the first PD fails with lower photocurrent. Nevertheless, the total photocurrent in a continuous mesa device is higher because multiple PDs in each array contribute to the total photocurrent. This explains why the wide-mesa device does not fail, even with a photocurrent of 16 mA, whereas continuous-mesa devices fail with a photocurrent of 7 or 8 mA in the first PD. In Section IV, we explained how high heat dissipation in the active region of the PD increases the dark current and leads to a catastrophic damage of the device.

The average responsivity is found to be  $\sim 0.35\text{ A/W}$  at 4-V bias [without antireflection (AR) coating] with 12 pairs of PDs in a receiver. The coupling efficiency of the lensed fibers in our setup was calculated to be  $\sim 50\%$ . In addition to low fiber-to-chip coupling efficiency, lossy sidewalls of the deeply etched WGs contributed to a low responsivity. We used a theoretical model to fit the experimental data and find the loss coefficients. In a distributed photodetection scheme, the input power is evanescently coupled to individual PDs from an optical WG. In this scheme, the total loss consists of loss in the optical WG and loss in the interface between the passive WG and active PDs. In the theoretical model, we used the experimentally observed fact that the responsivity saturates with 12 PDs in the receiver, as is shown in Fig. 6. The simulated quantum efficiency (QE) with different magnitude of loss coefficients per period (one period consists of a passive WG and two PD-WG interfaces) is shown in Fig. 7. When there is negligible loss, the QE tends to reach 50% (with 50% fiber-to-chip coupling loss). It is evident from Fig. 7 that, for any value of the loss coefficient, the QE flattens with  $\sim 12$  pairs of PDs in the receiver. The lowest curve in the figure corresponds to 3% loss per period and a quantum efficiency of  $\sim 28\%$ , which is the experimentally observed QE of our receiver at  $1.55\text{-}\mu\text{m}$  wavelength. The QE can be improved by

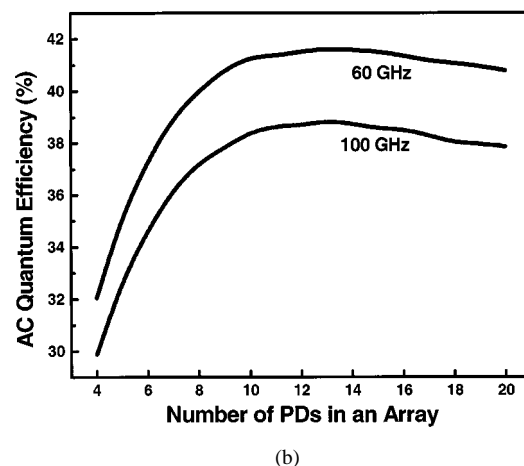
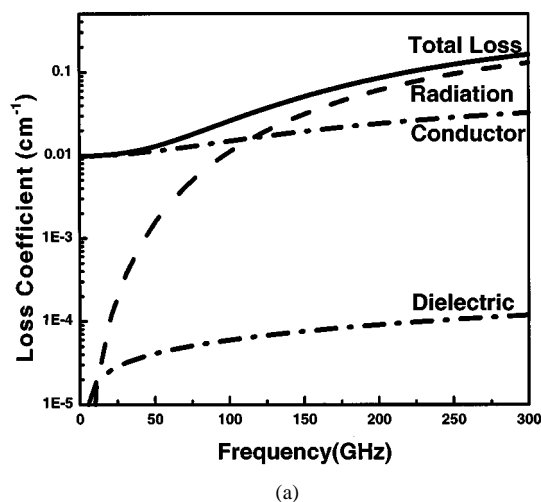


Fig. 8. (a) Three major contributors to the RF loss versus RF frequencies. (b) ac response versus length of receiver for 60-GHz and 100-GHz frequencies. The response first increases with increasing length of the receiver (because photocurrents are added in-phase) and then decreases when the length exceeds a certain limit, owing to the RF loss of the CPW. In the simulation, it is considered that 50% of the generated RF power goes to the input end termination resistor.

optimizing the coupling efficiency of the lensed fiber using spot-size converting technique [9], as well as by optimizing the WG etching process to generate smoother sidewalls.

Once good guiding and better distribution of input power is achieved, it is important to find the total physical length of the receiver that results in the optimum ac performance. In our receiver, a separate microwave transmission line (CPW) is employed to collect the AC signal from the array of balanced detectors. Like all other microwave transmission lines, CPW shows a certain amount of RF loss consisting of conductor, radiation, and dielectric losses [10]–[14]. Fig. 8(a) shows three major contributors to the total RF loss per unit length versus RF frequencies. With increasing frequencies of operation, the calculated RF loss in a transmission line increases almost exponentially. In our device, the period of balanced photodetector pair is  $120\text{ }\mu\text{m}$ . Each pair of balanced PDs is connected to the CPW by a metal interconnect of  $20\text{-}\mu\text{m}$  width. The thickness of the CPW metal is  $0.35\text{ }\mu\text{m}$ . By allowing a velocity mismatch of 1%, we simulated the ac quantum efficiencies for different lengths of receiver. Fig. 8(b) shows how ac response varies with different receiver size for 60-GHz and 100-GHz frequencies. The response

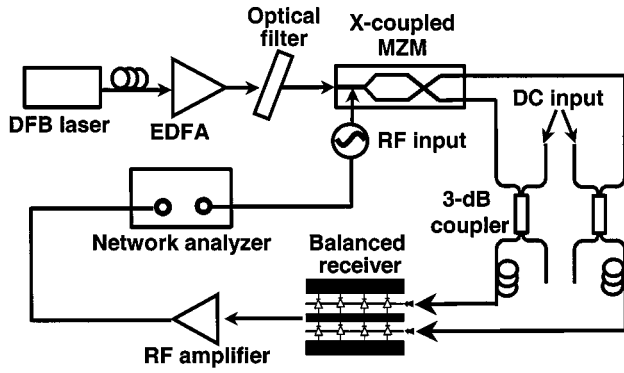


Fig. 9. Setup for measuring the nonlinearity of the distributed balanced receiver. The Mach-Zehnder modulator (MZM) output is kept at constant level, whereas the dc input from the 3-dB couplers is varied to increase the dc photocurrents.

first increases with increasing length of the receiver (because photocurrents are added in-phase) and then decreases when the length exceeds a certain limit, owing to the RF loss of the CPW. At high frequencies of operation, total RF loss in a transmission line is higher than that of lower frequencies of operation. This imposes a restriction on the total length of a device for each frequency of operation in order to keep the RF loss below a reasonable level. For a 100-GHz application, the optimum receiver size is  $\sim 1.5$  mm, which corresponds to 12 pairs of PDs in the receiver (with a period of  $120 \mu\text{m}$ ). For lower frequencies of operation, the length of the device for optimum RF response can be longer because the RF loss at lower frequencies is lower. For example, the device length can be 1.8 mm for a device designed for 60-GHz application. Note that total number of PDs per array (12 PDs) for optimum RF performance coincides with the total number of PDs for the saturation of responsivity in our device (shown in Fig. 6). Thus, the distribution of input power meets the requirements of device length for optimum ac response.

We previously mentioned about the requirements of matching the group velocity of the microwave signal to the velocity of the optical signal. However, in a multimode WG, different mode propagates at different velocities. Thus, the microwave velocity can only be matched to the group velocity of only one optical mode. Therefore, there is some inherent velocity mismatch in multimode devices. However, the mismatch is small ( $< 10\%$ ) and the bandwidth limit due to velocity mismatch is greater than 150 GHz, which is much higher than the transit time-limited bandwidth of our current device. When the design target goes above 100 GHz, single-mode WG will ensure better performance.

### III. MEASUREMENTS FOR AC LINEARITY

The optimized continuous-mesa receiver not only improved the DC linearity but also improved the RF performance significantly. In most of the reported photodetectors, nonlinear distortions are observed in photodetectors with photocurrents greater than a couple of milliamperes [15], [16]. Nonlinear distortions are attributed to high density of photogenerated carriers at high optical power, which results in nonlinear carrier velocity and, thus, saturation in the dc photocurrent level [15]. The saturation in the photocurrent results in a reduction in the RF current,

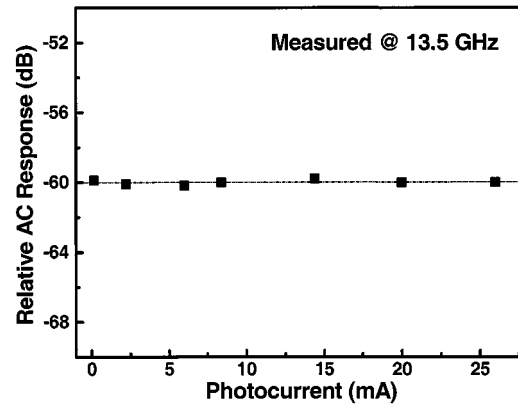


Fig. 10. Measured ac response of the balanced receiver at different photocurrent level. The response is linear at the shown photocurrent range within an experimental error of 0.5 dB.

reduced bandwidth, and sharp increase in harmonic distortion. Distortion is also observed at low optical power due to a change in photodetector impedance [16]. All of these can severely affect the performance of a high-power fiber optical link.

Liu *et al.* studied the difference between time domain and frequency domain nonlinear response mechanism of PDs, correlated both of them, and suggested frequency-domain measurement for the characterization of PDs that are intended to be used in RF links [17]. In order to investigate the ac linearity of the receiver, we employed three different approaches, all in frequency domain. First, we designed a setup, as depicted in Fig. 9, and varied the dc input power while keeping the ac input constant. At very high input power, buildup of carrier in the depletion region accompanied by a partial collapse of the depletion region electric field causes the ac response to decrease if the receiver does not have good ac linearity. A 1-dB compression current ( $I_{1\text{-dB}}$ ) is a good figure of merit proposed by Williams and Esman [18] to characterize the ac linearity of high power PDs. Our setup was also designed to investigate  $I_{1\text{-dB}}$  of the balanced receiver when biased in balanced mode.

In our setup, an external cavity tunable laser with 1550-nm wavelength and 3-dBm output power is employed as the optical source. It is amplified by an EDFA and then filtered by an optical bandpass filter with 2-nm bandwidth. The microwave signal was modulated onto the optical carrier by an X-coupled Mach-Zehnder modulator (MZM), which produces two complimentary outputs. The outputs are coupled to the balanced receiver by two lensed fibers. Another distortion-free external cavity laser is employed to provide additional dc input. It is similarly amplified by another EDFA, split into two equal branches, and then combined with the AC signals through two 3-dB couplers. The wavelengths of the external cavity lasers are separated far enough to avoid interference of their beating frequency. The polarization orientations of both ac and both dc signals are independently optimized by four polarization controllers. The effective ac photocurrents of the receiver was set to  $320 \mu\text{A}$  for each branch and the dc currents were allowed to vary from 0.3 mA to 26 mA (limited by our setup). Because  $I_{1\text{-dB}}$  is a function of the RF frequency, a frequency near the 3-dB bandwidth of the receiver electrical response (13.5 GHz) is chosen. Fig. 10 shows the ac output power versus the dc photocurrent at a frequency

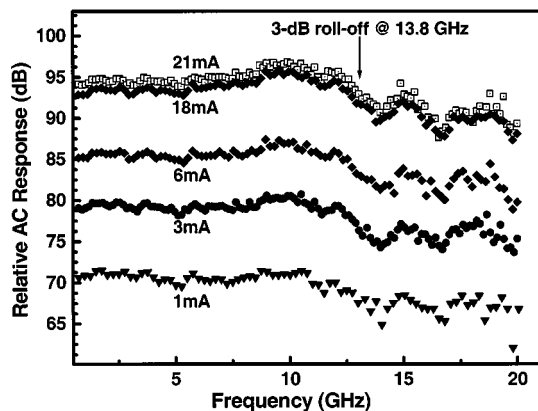


Fig. 11. Measured frequency response of the distributed balanced receiver at various dc photocurrents. The frequency response at 21 mA is identical to that at 1 mA, indicating excellent linearity of the balanced receiver at high photocurrent.

of 13.5 GHz. In this photocurrent range, the ac signal remained unchanged in magnitude within an experimental error of 0.5 dB. To our knowledge, this is the first report of the ac linearity measurement of balanced receivers.

To investigate the bandwidth performance of our receiver at high photocurrents, we used a similar setup, shown in Fig. 9, with several different input powers that go into the MZM. In this setup, both dc and ac input are varied simultaneously. We first measured the frequency response of a single branch of the photodetector by illuminating only one optical WG of the receiver with varying optical input powers. The bandwidth of the photodetector remained unchanged (14.5 GHz) when the photocurrent was varied from 0.5 mA to 15 mA on each branch. We then illuminated both of the optical WGs of the receivers, and biased the receiver in balanced mode and measured the ac response of the receiver at various photocurrent levels. Fig. 11 shows the relative ac responsivity of the balanced receiver with effective photocurrents varied from 1 mA to 21 mA. The frequency response at 21 mA is identical to that at 1 mA, indicating excellent linearity of the receiver at high photocurrent. The 3-dB bandwidth of the balanced receiver (13.8 GHz) is slightly lower than that of the individual branches (14.5 GHz). This may be due to parasitics of the biasing capacitor (120 pF) on one ground of the probe for dc biasing and RF signal collection.

Fig. 12 shows the ac response of the receiver at RF frequencies of 10 and 15 GHz versus the dc photocurrents. The ac response is proportional to the square of the photocurrent up to the highest photocurrent measured (21 mA, limited by the setup). This confirms the linearity of the photodetector and demonstrates the effectiveness of distributed detection.

#### IV. CORRELATION BETWEEN DARK CURRENT AND PHOTOCURRENT AT FAILURE

There have been several investigations on the failure mechanism and thermal management of high-power PDs. Although considerable power levels in the PDs have been achieved by several researchers [4], [19]–[23], long-term reliability of high power PDs is still an unsolved issue. Therefore, it is important to have a clear understanding of the factors that contribute

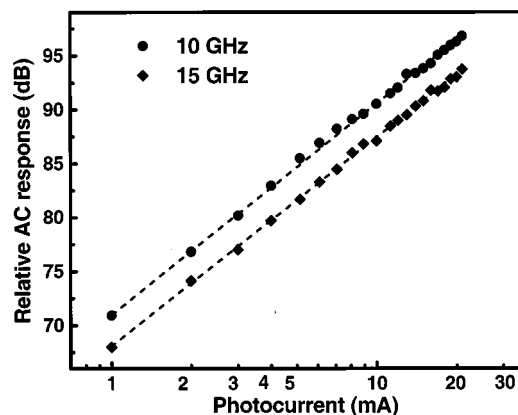


Fig. 12. Measured ac linearity of the balanced receiver at different photocurrents. The dotted line shows the ideal linearity curves.

to the failure mechanism of the PDs at high power operation. Williams and Esman compared surface-illuminated and waveguide PDs and showed that waveguide PDs have advantages over surface-illuminated PDs because the thermal impedance due to the heat source in the former is long and narrow [24]. In this context, distributed photodetectors are even superior in performance because the heat is further distributed in much longer length. Paslaski *et al.* studied p-i-n PDs and suggested a failure mechanism of high power PDs, relating it to the thermal origin [23]. Investigations carried out by Nespola *et al.* on MSM-based distributed PDs confirmed the suggestion that PDs fail along curves of constant power dissipation [8]. However, none of the previous investigations have tried to correlate the dark current at room temperature to the photocurrent level at failure. Here, we report our work on the experimental investigation of the role of  $I_d$  on the failure mechanism of high power PDs. A theoretical model built to fit the experimental data indicates that the  $I_d$  and the effective barrier height ( $q\phi_b$ ) are the fundamental parameters in the failure mechanism of high power PDs. Our investigation also shows that junction PDs (such as p-i-n) with high  $q\phi_b$  are expected to perform better than metal–semiconductor contact PDs (such as MSM or Schottky) when high power operation is considered.

In order to demonstrate a relationship between the maximum photocurrent at failure and the  $I_d$ , we tested several structures with varying  $I_d$  levels. To make a fair comparison, we chose two groups of structures—one with very low  $I_d$  (PD1) of  $\sim 0.1$  nA per diode ( $0.26$  pA/ $\mu\text{m}^2$ ) and the other (PD2) with high  $I_d$  of  $\sim 33$  nA per diode ( $85$  pA/ $\mu\text{m}^2$ ). Both groups of photodetectors consist of continuous optical WGs, are monolithically fabricated on the same wafer, and exhibit high linear photocurrents. The variation in dark currents is caused by surface treatment before evaporation of the Schottky metals. Measurements of  $I_d$  were performed from 2 V–12 V at temperatures ranging from 20 to 95 °C. Fig. 13 shows the  $I_d$  of both groups of devices (one sample from each group) with 11 pairs of PDs on each structure versus temperature  $T$  at 4-V bias. Note that at low temperature, the  $I_d$  is dominated by field emission (FE), and at high temperature by thermionic field emission (TFE). Two different slopes in Fig. 13 depict these two mechanisms.

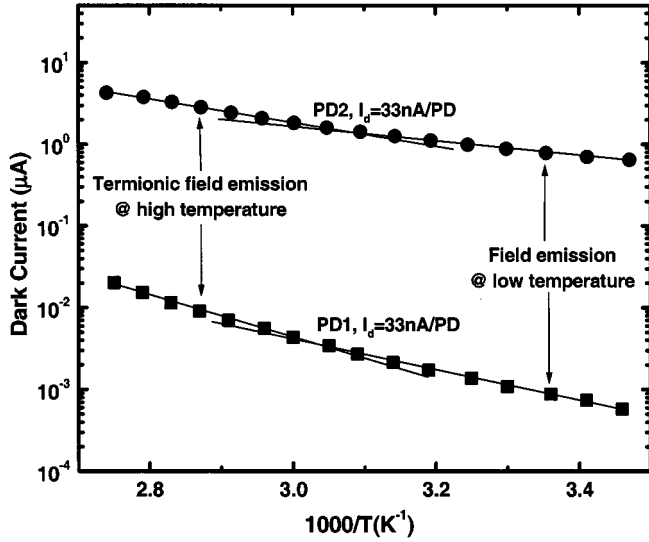


Fig. 13. Dark current of each PD from both groups of devices (PD1 and PD2) versus temperature at 4-V bias. At low temperature, the  $I_d$  is dominated by field emission, and at high temperature by thermionic field emission. Two different slopes in both sets of data depict these two mechanisms.

TABLE I  
CHARACTERISTICS OF DEVICES USED IN THE FAILURE ANALYSIS

Device	$I_d$ /PD (T=0°C)	$I_d$ /PD (T=95°C)	Photocurrent at Failure	Dissipated Power	$q\phi_b$ (eV)
PD1	0.1nA	.015μA	33mA	~132mW	0.43eV
PD2	33nA	3.8μA	17mA	~70mW	0.32eV

When these two groups of PDs are tested for their photocurrent levels, it was found that PD1 fails with a photocurrent of 33 mA on each branch when biased at 4 V, generating a thermal power of 132 mW (as shown in Fig. 5). A large number of PDs with similar  $I_d$  levels were found to dissipate this amount of power at the time of failure. PD2, on the other hand, fails with an average photocurrent of ~17 mA (with ~70-mW power). Note that, although both types of PDs are monolithically fabricated on the same wafer and are designed to reach high photocurrent levels, one group with high  $I_d$  fails at much lower photocurrents than the other. Our measurements indicate that PDs fail along curves of constant power dissipation only when they have identical  $I_d$  at room temperature. Multiple diodes with high  $I_d$  levels were tested to reach this conclusion. Table I summarizes the characteristics of the devices that we tested.

The measured  $I_d$  of our MSM based PDs is expected to obey a behavior of the form

$$J_{\text{dark}} = J_s \exp\left(\frac{-qV}{nK_B T}\right) \left[ \exp\left(\frac{qV}{K_B T}\right) - 1 \right]$$

where

$$J_s = A^{**} T^2 \exp\left\{\frac{-q\phi_b}{K_B T}\right\} \propto \exp\left\{\frac{-q\phi_b}{K_B T}\right\}. \quad (1)$$

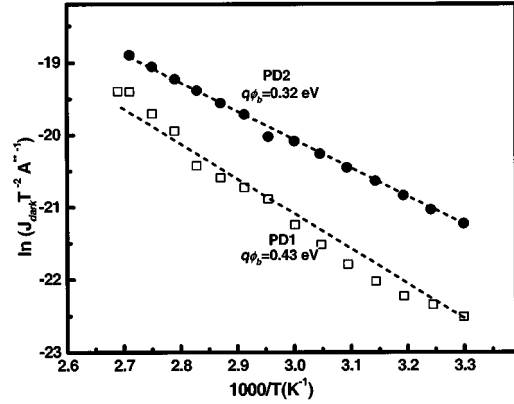


Fig. 14. Experimental data are fitted to the theoretical model (dotted lines) in order to extract the value of effective barriers ( $q\phi_b$ ). The magnitude of dark currents at different temperature depends on effective barrier height ( $q\phi_b$ ).

In (1),  $n$  is the ideality factor,  $A^{**}$  is the Richardson constant, and  $q\phi_b$  is the effective barrier of metal–semiconductor junction. Because of localized surface states,  $q\phi_b$  is always lower than the  $E_g$ , the bandgap of the semiconductor. Using Bardeen's approximation [25], we can write  $q\phi_b \cong 2/3E_g$  in the ideal cases. Depending on the quality of the surface and process parameters,  $q\phi_b$  can be even lower in values. We used a theoretical model built around (1) to have a linear fit of both sets of data. The slopes of the fitted data (shown in Fig. 14) give the effective barrier heights of each type of PDs, which are 0.43 eV for PD1 (PD with low  $I_d$ ) and 0.32 eV for PD2 (PD with high  $I_d$ ).

It has been shown that photocurrent causes joule heating in the active region of a PD [8]. Our theoretical model shows that a temperature rise in the PDs almost exponentially increases the  $I_d$  and causes additional increase in the diode temperature, resulting in an additional  $I_d$  [23]. This positive thermal feedback process continues until the PDs fail. The failure mechanism is accelerated for PDs with low value of  $q\phi_b$ . From (1), it is evident that PDs with high  $I_d$  are expected to have lower  $q\phi_b$  and enter the feedback loop at lower temperature. We have experimentally observed that PDs with high  $I_d$  fail at much lower photocurrent than PDs with low  $I_d$ .

Our investigation leads to the following conclusions.

- 1) Dark current plays an important role in the reliability of high power PDs.
- 2) Diodes with low dark currents and high effective barriers are expected to sustain larger amount of Joule heating.

Thus, it is important to screen PDs on dark currents for good reliability under high power operation. These observations are significant for understanding the catastrophic failure of high power PDs.

The dark current density  $J_{\text{dark}}$  and reverse saturation current density  $J_{\text{sat}}$  for junction diode (such as p-i-n) is related to the bandgap  $E_g$  as the following expression:

$$J_{\text{dark}} = J_s \left[ \exp\left(\frac{qV}{K_B T}\right) - 1 \right]$$

where

$$J_{\text{sat}} = \left[ \frac{qD_p p_{n0}}{L_p} + \frac{qD_n n_{p0}}{L_n} \right] \propto \exp\left[\frac{-E_g}{K_B T}\right] \quad (2)$$

where

- $D_n$  electron diffusion coefficient;
- $D_p$  hole diffusion coefficient;
- $n_{p0}$  equilibrium concentration of electrons in  $p$  region;
- $p_{p0}$  equilibrium concentration of holes in  $n$  region;
- $L_n$  electron diffusion length;
- $L_p$  hole diffusion length;
- $K_B$  Boltzman constant.

Careful investigation into the reverse saturation current expression for both Schottky and p-i-n diodes from (1) and (2) reveals that effective barrier of a p-i-n PD is always equal to the semiconductor bandgap ( $E_g$ ) in the ideal case. Impurity-induced trapped sites in the forbidden gap may slightly lower the barrier in the real devices. Metal–semiconductor contact, on the other hand, has much lower effective barrier, as mentioned previously. Because of these fundamental differences in the characteristics and effective barrier height, the p-i-n PD is ideally expected to have more than five orders of magnitude lower dark currents than a PD with metal–semiconductor contact of equal active areas. Furthermore, it was shown that PDs with metal–semiconductor contact fail when the device temperature reaches 700 K [8], whereas junction diodes like p-i-n can stand temperature above 900 K [23]. Considering all of these factors, it is concluded that p-i-n PDs offer fundamental advantages for high power applications.

## V. CONCLUSION

We have successfully demonstrated a distributed balanced photodetector with high photocurrent and excellent linearity. It has a maximum linear dc photocurrent of 33 mA (equivalent to 66 mA in single-ended photodetectors). The device also exhibited excellent ac linearity at high photocurrent. Distributed detection is measured experimentally for the first time and is shown to be important for high power linear photodetectors. A correlation between the dark current and the failure mechanism has been established. The experimental results indicate that the distributed balanced photodetector will have a major impact on high performance RF photonic systems.

The understanding related to the failure mechanism and true distribution of input power are going to be helpful in our future plans. In order to increase the photocurrent to further higher level with higher bandwidth, we are currently working on p-i-n PD to design distributed balanced receiver. We are also working on implementing a laterally multimode WG with large core size in order to increase the quantum efficiency of the receiver [26]. Spot-size converters can further increase the fiber coupling efficiency [9]. We recently achieved 45 mA of linear photocurrent in velocity-matched distributed photodetector (VMDP) with p-i-n PDs. The devices did not fail even with a DC photocurrent as high as 55 mA [27]. The higher effective barrier height of p-i-n PD helped improve the failure photocurrent level dramatically. This observation validates our described failure analysis on higher power photodetectors. A device with 100-GHz bandwidth and 100 mA of effective dc photocurrent appears to be feasible with p-i-n PDs.

## ACKNOWLEDGMENT

The authors wish to thank S. Mathai and M. Yeahia of University of California-Los Angeles (UCLA), Los Angeles, CA, for their help during the experiments and S. Murthy of UCLA and Dr. T. Chau of Tellium, Inc., West Long Branch, NJ, for their help in the design and simulations.

## REFERENCES

- [1] C. H. Cox III, G. E. Betts, and L. M. Johnson, "An analytic and experimental comparison of direct and external modulation in analog fiber-optic links," *IEEE Trans. Microwave Theory Tech.*, vol. 38, pp. 501–509, May 1991.
- [2] L. T. Nichols, K. J. Williams, and R. D. Esman, "Optimizing the ultrawideband photonic link," *IEEE Trans. Microwave Theory Tech.*, vol. 45, pp. 1384–1389, Aug. 1997.
- [3] M. S. Islam, T. Chau, A. Nespola, S. Mathai, A. R. Rollinger, W. R. Deal, T. Itoh, M. C. Wu, D. L. Sivco, and A. Y. Cho, "Distributed balanced photodetectors for high performance RF photonic links," *IEEE Photon. Technol. Lett.*, vol. 11, pp. 457–560, Apr. 1999.
- [4] L. Y. Lin, M. C. Wu, T. Itoh, T. A. Vang, R. E. Muller, D. L. Sivco, and A. Y. Cho, "High-power high-speed photodetectors- design, analysis and experimental demonstration," *IEEE Trans. Microwave Theory Tech.*, vol. 45, pp. 1320–1331, Aug. 1997.
- [5] M. S. Islam, T. Chau, S. Mathai, T. Itoh, M. C. Wu, D. L. Sivco, and A. Y. Cho, "Distributed balanced photodetectors for broadband noise suppression," *IEEE Trans. Microwave Theory Tech.*, pp. 1282–1288, July 1999.
- [6] W. Ng, A. Narayanan, R. R. Hayes, D. Persechini, and D. Yap, "High efficiency waveguide-coupled  $\lambda = 1.3 \mu\text{m}$  In<sub>x</sub>Ga<sub>1-x</sub>As/GaAs detector exhibiting large extinction ratios at L and X band," *IEEE Photon. Technol. Lett.*, vol. 5, pp. 514–517, May 1993.
- [7] W. A. Wohlmuth, P. Fay, and I. Adesida, "Dark current suppression in GaAs metal-semiconductor-metal photodetectors," *IEEE Photon. Technol. Lett.*, vol. 8, pp. 1061–1064, Aug. 1996.
- [8] A. Nespola, T. Chau, M. Pirola, M. C. Wu, G. Ghione, and C. U. Naldi, "Failure analysis of travelling wave MSM distributed photodetectors," in *Proc. Int. Electron Devices Annu. Meeting*, San Francisco, CA, Dec. 6–9, 1998, pp. 69–72.
- [9] A. Umbach, D. Trommer, R. Steingruber, A. Seeger, W. Ebert, and G. Unterborsch, "Ultrafast, high-power 1.55  $\mu\text{m}$  side-illuminated photodetector with integrated spot size converter," in *Proc. OFC 2000*, Baltimore, MD, Mar. 7–10, 2000, pp. 117–119.
- [10] I. J. Bahl, "Design Considerations for Coplanar Waveguides and Coplanar Strips," *Elect. Eng. Dept.*, Indian Institute of Technology, Kanpur, India, vol. 78-MW1, 1978.
- [11] M. E. Davis, E. W. Williams, and A. C. Celestini, "Finite-boundary corrections to the coplanar waveguide analysis," *IEEE Trans. Microwave Theory Tech.*, vol. 21, pp. 594–596, Sept. 1973.
- [12] G. Hasnain, A. Dienes, and J. R. Whinnery, "Dispersion of picosecond pulses in coplanar transmission lines," *IEEE Trans. Microwave Theory Tech.*, vol. 34, pp. 738–741, June 1989.
- [13] M. Y. Frankel, S. Gupta, J. A. Valdmanis, and G. A. Mourou, "Terahertz attenuation and dispersion characteristics of coplanar transmission lines," *IEEE Trans. Microwave Theory Tech.*, vol. 39, pp. 910–916, June 1991.
- [14] C. P. Wen, "Coplanar waveguide: A surface strip transmission line suitable for nonreciprocal gyromagnetic device application," *IEEE Trans. Microwave Theory Tech.*, vol. MTT-17, pp. 1087–1090, 1969.
- [15] K. J. Williams and R. D. Esman, "Photodiode dc and microwave nonlinearity at high currents due to carrier recombination nonlinearities," *IEEE Photon. Technol. Lett.*, vol. 10, pp. 1015–1018, July 1998.
- [16] H. Jian and P. K. L. Yu, "Equivalent circuit analysis of harmonic distortions in photodiode," *IEEE Photon. Technol. Lett.*, vol. 10, pp. 1608–1611, Nov. 1998.
- [17] P.-L. Liu, K. J. Williams, M. Y. Frankel, and R. D. Esman, "Saturation characteristics of fast photodiodes," *IEEE Trans. Microwave Theory Tech.*, vol. 47, pp. 1297–1303, July 1999.
- [18] K. J. Williams and R. D. Esman, "Optically amplified downconverting link with shot-noise-limited performance," *IEEE Photon. Technol. Lett.*, vol. 8, pp. 148–150, Jan. 1996.
- [19] A. R. Williams, A. L. Kellner, X. S. Jiang, and P. K. L. Yu, "InGaAs/InP waveguide photodetector with high saturation intensity," *Electron. Lett.*, vol. 28, pp. 2258–2260, Nov. 1992.

- [20] S. Jasmin, N. Vodjdani, J.-C. Renaud, and A. Enard, "Diluted and distributed-absorption microwave waveguide photodiodes for high efficiency and high power," *IEEE Trans. Microwave Theory Tech.*, vol. 45, pp. 1337–1341, Aug. 1997.
- [21] K. S. Giboney, M. J. W. Rodwell, and J. E. Bowers, "Travelling-wave photodetector theory," *IEEE Trans. Microwave Theory Tech.*, vol. 45, pp. 1310–1319, Aug. 1997.
- [22] C. L. Goldsmith, G. A. Magel, and R. J. Boca, "Principals and performance of travelling-wave photodetector arrays," *IEEE Trans. Microwave Theory Tech.*, vol. 45, pp. 1310–1319, Aug. 1997.
- [23] J. Paslaski, P. C. Chen, J. S. Chen, C. M. Gee, and N. Bar-Chaim, "High-power microwave photodiode for improving performance of RF fiber optic links," in *Proc. SPIE, Photon. Radio Freq.*, vol. 2844, Denver, CO, 1996, pp. 110–119.
- [24] K. J. Williams and R. D. Esman, "Design considerations of high-current photodetectors," *J. Lightwave Technol.*, vol. 17, pp. 1443–1454, Aug. 1999.
- [25] M. S. Tyagi, *Introduction to Semiconductor Materials and Devices*. New York: Wiley, 1991, pp. 275–276.
- [26] K. Kato, S. Hata, K. Kawano, J. Yoshida, and A. Kozen, "A high efficiency 50 GHz InGaAs multimode waveguide photodetector," *IEEE J. Quantum Electron.*, vol. 28, pp. 2728–2735, Dec. 1992.
- [27] M. S. Islam, S. Murthy, T. Itoh, M. C. Wu, D. Novak, R. B. Waterhouse, D. L. Sivco, and A. Y. Cho, *IEEE Trans. Microwave Theory Tech.*, vol. 49, pp. 1914–1920, Oct. 2001.



**M. Saif Islam** (S'98–M'02) received the B.Sc. degree in physics from Middle East Technical University (METU), Ankara, Turkey, in 1994 and the M.Sc. degree in physics from Bilkent University, Ankara, Turkey, in 1996. He received the M.S. and Ph.D. degrees in electrical engineering from the University of California at Los Angeles (UCLA), Los Angeles, in 1999 and 2001, respectively.

He joined the Integrated Photonics Laboratory at UCLA in 1997. In January 2001, he joined SDL, Inc., Santa Clara, CA, as a Research Scientist

with the Technology Development Group. After the merger of SDL, Inc., with JDS Uniphase Corporation, he was with the Optical Network Research Group at Santa Clara, CA, where he conducted research on return-to-zero (RZ) transmission systems and issues related to Raman pump modules. Currently, he is with Gazillion Bits, Inc., San Jose, CA. He has published more than 30 papers in technical journals and refereed conferences and contributed one book chapter. His research interests include design, fabrication, and characterization of ultrafast resonant cavity enhanced photodetectors; high-power and high-bandwidth photodetectors; integrated optoelectronic devices; integrated microwave photonic devices including velocity-matched distributed photodetectors (VMDP); and distributed balanced photodetectors and their applications in high performance RF photonic systems.

Dr. Islam is a member of the Optical Society of America (OSA) and the American Physical Society. In 1998, he received the Student of the Year Award from the Bangladesh National Student Foundation. In 1989, he received the Chancellor's Award for securing the first position in the HSC examination among all education boards in Bangladesh. He held the UCLA Chancellor's Dissertation Year Fellowship from 2000 to 2001. He is a recipient of the 2000 IEEE Laser and Electro-Optics Society (LEOS) Graduate Student Fellowship Award.

**Thomas Jung** (S'87) received the B.S. and M.S. degrees in electrical engineering from the University of California at Los Angeles (UCLA), Los Angeles, in 1996 and 1998, respectively. He is currently pursuing the Ph.D. degree at UCLA under Dr. M. C. Wu.

From 1996 to 1998, he was a Member of the Technical Staff of the Photonics Technology Department, TRW, Inc. His research interests include modeling of high-speed photonic devices, laser modeling, RF photonics, ultrafast lasers, and electrooptic sampling of high-speed photonic devices.



**Tatsuo Itoh** (S'69–M'69–SM'74–F'82) received the Ph.D. degree in electrical engineering from the University of Illinois, Urbana, in 1969.

From September 1966 to April 1976, he was with the Electrical Engineering Department, University of Illinois. From April 1976 to August 1977, he was a Senior Research Engineer in the Radio Physics Laboratory, SRI International, Menlo Park, CA. From August 1977 to June 1978, he was an Associate Professor at the University of Kentucky, Lexington. In July 1978, he joined the faculty at the University of Texas, Austin, where he became a Professor of Electrical Engineering in 1981 and Director of the Electrical Engineering Research Laboratory in 1984. During the summer of 1979, he was a Guest Researcher at AEG-Telefunken, Ulm, West Germany. In September 1983, he was selected to hold the Hayden Head Centennial Professorship of Engineering at the University of Texas. In September 1984, he was appointed Associate Chairman for Research and Planning of the Electrical and Computer Engineering Department at the University of Texas. In January 1991, he joined the University of California-Los Angeles (UCLA), Los Angeles, as Professor of Electrical Engineering and holder of the TRW Endowed Chair in Microwave and Millimeter Wave Electronics. He was an Honorary Visiting Professor at Nanjing Institute of Technology, Nanjing, China, and at Japan Defense Academy, Yokosuka, Japan. In April 1994, he was appointed as Adjunct Research Officer for Communications Research Laboratory, Ministry of Post and Telecommunication, Japan. He currently holds Visiting Professorship at University of Leeds, Leeds, U.K., and is an External Examiner of Graduate Program of City University of Hong Kong, Kowloon, Hong Kong. He served as the Editor-in-Chief of IEEE TRANSACTIONS ON MICROWAVE THEORY AND TECHNIQUES from 1983 to 1985. He serves on the Administrative Committee of the IEEE Microwave Theory and Techniques Society. He was the Editor-in-Chief of IEEE MICROWAVE AND GUIDED WAVE LETTERS from 1991 to 1994. He was Vice President of the Microwave Theory and Techniques (MTT) Society in 1989 and President in 1990, and was elected as an Honorary Life Member of the MTT Society in 1994. He was the Chairman of USNC-International Scientific Radio Union (URSI) Commission D from 1988 to 1990 and Chairman of Commission D of URSI for 1993 to 1996, and is the current Chair of the URSI Long Range Planning Committee. He serves on advisory boards and committees of a number of organizations. He has published 274 journal papers, made 540 refereed conference presentations, and written 30 books or chapters in the area of microwaves, millimeter-waves, antennas, and numerical electromagnetics. He has also overseen 49 Ph.D. students.

Dr. Itoh is a member of the Institute of Electronic, Information, and Communication Engineers (IEICE) of Japan, and Commissions B and D of USNC-URSI. He has received a number of awards, including the Shida Award from Japanese Ministry of Post and Telecommunications in 1998, the Japan Microwave Prize in 1998, the IEEE Third Millennium Medal in 2000, and the IEEE MTT Distinguished Educator Award in 2000.



**Ming C. Wu** (S'82–M'83–SM'00) received the M.S. and Ph.D. degrees in electrical engineering from the University of California at Berkeley, Berkeley, in 1985 and 1988, respectively.

From 1988 to 1992, he was a Member of Technical Staff at AT&T Bell Laboratories, Murray Hill, NJ, where he conducted research in high-speed semiconductor lasers and optoelectronics. In 1993, he joined the faculty of the Electrical Engineering Department, University of California at Los Angeles (UCLA), Los Angeles, and is currently Professor.

He is the Director of the Multi-University Research Institute (MURI) Center on RF Photonic Materials and Devices sponsored by the Office of Naval Research, and a member of California NanoSystem Institute (CNSI). His current research interests include microelectromechanical systems (MEMS), micro-opto-electro-mechanical systems (MOEMS), microwave photonics, and high-speed optoelectronics. He was General Co-Chair of the IEEE Lasers and Electro-Optics Society (LEOS) Summer Topical Meeting on RF optoelectronics in 1995 and on optical MEMS in 1996 and 1998, and General Co-Chair of the IEEE LEOS International Conference on MOEMS in 1998. He has also served on the Program Committees of OFC, CLEO, MEMS, Optical MEMS, IEDM, and DRC. He has published more than 100 journal papers and 180 conference papers, contributed one book chapter, and holds eight U.S. patents.

Dr. Wu is a member of the Optical Society of America (OSA), American Physical Society, URSI, and Eta Kappa Nu. He received the Packard Foundation Fellowship in 1992, and the Meritorious Conference Paper Award of 1994 GOMAC.

**Antonino Nespola**, photograph and biography not available at the time of publication.



**Deborah L. Sivco** received the B.A. degree in chemistry from Rutgers University, New Brunswick, NJ, in 1980, and the M.A. degree in materials science from Stevens Institute of Technology, Hoboken, NJ, in 1988.

In 1981, she joined Bell Laboratories, and is currently a Member of Technical Staff in the Semiconductor Research Laboratory, Bell Laboratories, Lucent Technologies, Murray Hill, NJ. Since 1981, she has been involved with molecular beam epitaxial (MBE) growth of III-V compounds.

She has performed the crystal growth of GaAs-AlGaAs and InGaAs-InAlAs heterostructures for field-effect transistors, resonant tunneling transistors, bipolar transistors, double heterostructure lasers, and detectors. She recently prepared the world's first quantum cascade laser, designed by Faist *et al.*, using bandgap engineering. She has coauthored 170 journal papers and holds nine patents.



**Alfred Y. Cho** (S'57-M'60-SM'79-F'81) was born in Beijing, China. He received the B.S., M.Sc., and Ph.D. degrees in electrical engineering from the University of Illinois, Urbana-Champaign.

In 1968, he joined Bell Laboratories as a Member of Technical Staff, and in 1984, he was promoted to Department Head. In 1987, he was Director of the Materials Professing Research Laboratory and, in 1990, he became Director of Semiconductor Research. Currently, he is the Semiconductor Research Vice President at Bell Laboratories, Lucent

Technologies, Murray Hill, NJ. His pioneering work on molecular beam epitaxy (MBE) has had a significant impact on the semiconductor industry, leading to the making of faster and more efficient electronic and optoelectronic semiconductor devices.

Dr. Cho is a member of the Chinese Academy of Sciences, Academia Sinica, Third World Academy of Sciences, American Academy of Arts and Sciences, National Academy of Engineering, National Academy of Sciences, and the American Philosophical Society. He is the recipient of a number of awards from technical and professional societies, including the 1982 International Prize for New Materials from the American Physical Society, the 1987 Solid State Science and Technology Medal of the Electrochemical Growth Award of the American Association for Crystal Growth, the 1993 National Medal of Science presented by President Clinton, the 1994 IEEE Medal of Honor, the 1995 Elliott Cresson Medal of the Franklin Institute, the 1995 Computer and Communications (C&C) Prize. He was inducted into the Japan and New Jersey Inventors Hall of Fame in 1997.